Resource

Structure

MonoRes: Automatic and Accurate Estimation of Local Resolution for Electron Microscopy Maps

Graphical Abstract

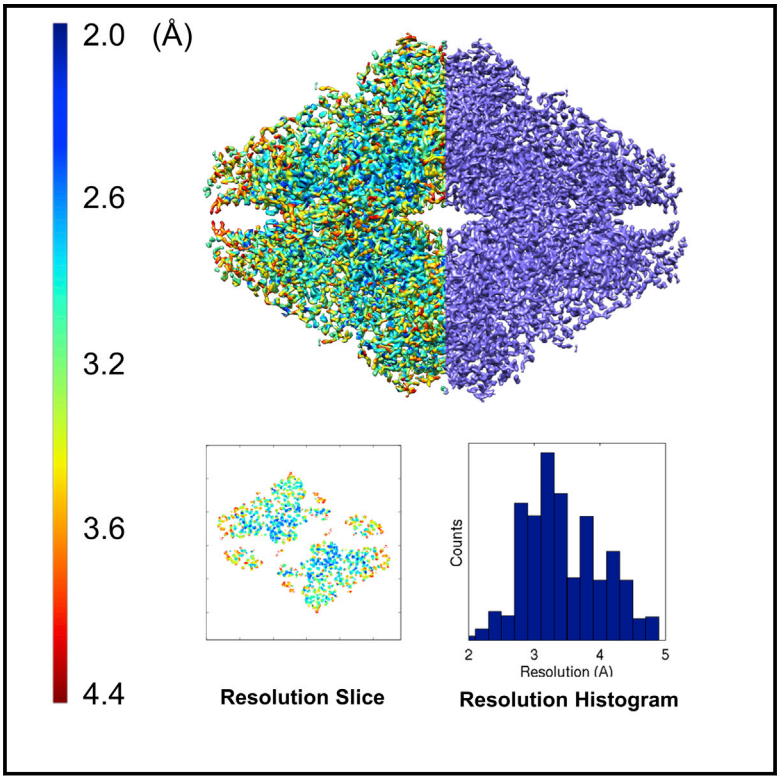

Authors

Jose Luis Vilas, Josué Gómez-Blanco, Pablo Conesa, ..., José María Carazo, Javier Vargas, Carlos Oscar S. Sorzano

Correspondence

jlvilas@cnb.csic.es (J.L.V.), carazo@cnb.csic.es (J.M.C.), coss@cnb.csic.es (C.O.S.S.)

In Brief

Vilas et al. present MonoRes, a fast and fully automatic method to determine the local resolution in electron density maps. It also allows local filtering of the original map at local resolution values.

Highlights

- Resolution is a local feature of electron density maps
- MonoRes provides a fast, automatic, and accurate estimation of resolution maps
- Local filtering of electron density maps is provided
- MonoRes method is invariant under b-factor and prewhitening correction

Vilas et al., 2018, Structure *26*, 337–344
February 6, 2018
https://doi.org/10.1016/j.str.2017.12.018

CellPress

Structure
Resource

MonoRes: Automatic and Accurate Estimation of Local Resolution for Electron Microscopy Maps

Jose Luis Vilas,[1,6,*] Josué Gómez-Blanco,[1] Pablo Conesa,[1] Roberto Melero,[1] José Miguel de la Rosa-Trevín,[2] Joaquin Otón,[1] Jesús Cuenca,[1] Roberto Marabini,[3] José María Carazo,[1,*] Javier Vargas,[4] and Carlos Oscar S. Sorzano[1,5,*]
[1]Biocomputing Unit, National Center for Biotechnology (CSIC), Darwin 3, Campus Universidad Autónoma, Cantoblanco, 28049 Madrid, Spain
[2]Science for Life Laboratory, Stockholm University, Stockholm, Sweden
[3]Escuela Politécnica Superior, Universidad Autónoma de Madrid, Cantoblanco, 28049 Madrid, Spain
[4]Department of Anatomy and Cell Biology, McGill University, University Street Strathcona Anatomy Building, 3640 Montreal, Canada
[5]Department of Engineering of Electronic and Telecommunication Systems, Universidad San Pablo-CEU, Campus Urbanización Montepríncipe, Boadilla del Monte, 28668 Madrid, Spain
[6]Lead Contact
*Correspondence: jlvilas@cnb.csic.es (J.L.V.), carazo@cnb.csic.es (J.M.C.), coss@cnb.csic.es (C.O.S.S.)
https://doi.org/10.1016/j.str.2017.12.018

SUMMARY

Since the beginning of electron microscopy, resolution has been a critical parameter. In this article, we propose a fully automatic, accurate method for determining the local resolution of a 3D map (*MonoRes*). The foundation of this algorithm is an extension of the concept of analytic signal, termed monogenic signal. The map is filtered at different frequencies and the amplitude of the monogenic signal is calculated, after which a criterion is applied to determine the resolution at each voxel. *MonoRes* is fully automatic without compulsory user parameters, with great accuracy in all tests, and is computationally more rapid than existing methods in the field. In addition, *MonoRes* offers the option of local filtering of the original map based on the calculated local resolution.

INTRODUCTION

The general goal of cryoelectron microscopy (cryo-EM) using single particle analysis (SPA) is to obtain the electron density map of a macromolecule or assembled complex, a crucial step in its characterization. The map thus obtained (a three-dimensional [3D] volume) is analyzed to assess its quality, for which resolution plays a central role since, in simple terms, resolution can be understood as the size of the smallest reliable detail in the map. A number of studies have addressed the issue of how to estimate map resolution, such as Fourier shell correlation (FSC) (Saxton, 1978; Saxton and Baumeister, 1982; Harauz and van Heel, 1986), spectral signal-to-noise ratio (Unser et al., 1987, 2005; Penczek, 2002), Fourier neighbor correlation (Sousa and Grigorieff, 2007), and differential phase residual, among others (for a thorough review of these methods, see Sorzano et al., 2017).

The most common approach to estimating resolution in SPA is the FSC, which calculates the normalized cross-correlation between two maps at different frequencies (maps are normally reconstructed using two halves of the data). The FSC is thus a self-consistency measurement, although it is usually quoted as a resolution estimation. SPA reconstruction ideally considers that all images are projections of the same complex (in the absence of flexibility) and that the angular projection space is well covered. A perfect reconstruction should therefore present the same degree of detail for any direction and any location. Reality is nonetheless different. Particles might not be exactly the same, for example, since there can be some heterogeneity in the macromolecules being imaged, due to radiation damage, or even the flexibility of the structure. Moreover, the angular orientation and in-plane alignment of the particles used for the reconstruction might be identified incorrectly, or the data might have a non-uniform orientation distribution pattern (Sorzano et al., 2001). The result is an electron density map in which different regions can differ markedly in quality. Most methods for determining map resolution are global and do not take into account such local or orientation-related differences.

One of the first attempts to define a local resolution estimation was *blocres* (Cardone et al., 2013), in which the FSC between two maps was calculated by extracting small patches from these volumes. The method uses a moving window and computes the FSC within it. Its main drawbacks are the need to adjust window size and to use two half-maps.

The state of the art in local resolution estimation is currently dominated by *ResMap* (Kucukelbir et al., 2014). It is founded on detection of a 3D sinusoidal wave above the noise level for each map point, an approach that a large body of experience in cryo-EM-SPA has certainly validated, at least in general terms. A number of *ResMap* limitations motivated our work, such as the need for an initial step in which the user must manually find a frequency transformation that produces a flat spectrum within a given frequency region; in addition, the method lacks a structural map output locally filtered to the estimated local resolution. It is also difficult to conduct certain defined accuracy tests with fine resolution discrimination that would allow analysis of possible over- or underestimation. Moreover, we wanted to develop a more rapid, computationally less-demanding approach that, coupled with full automation and the ability to produce a locally filtered map, could lead to new uses and possibilities, for instance, by forming part of iterative approaches to refinement or fitting/modeling.

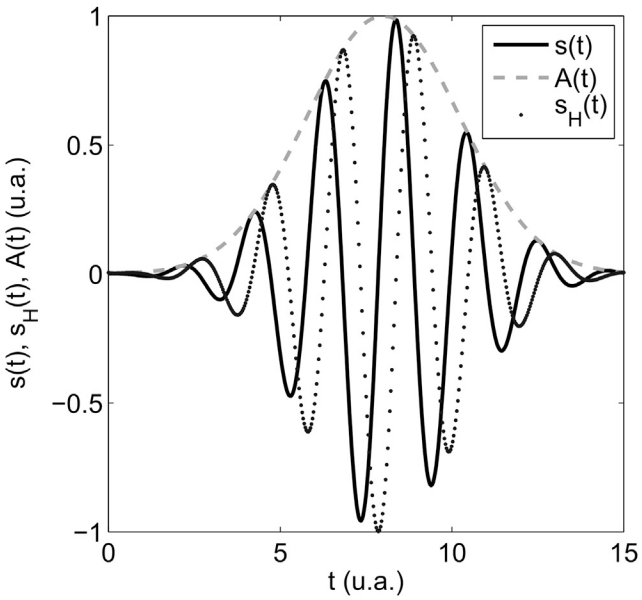

Figure 1. Signal Decomposition

From an Original Signal s(t) (continuous), the Hilbert Transform is calculated (dotted) and the Amplitude or Envelope of the Analytic Signal is shown (dashed).

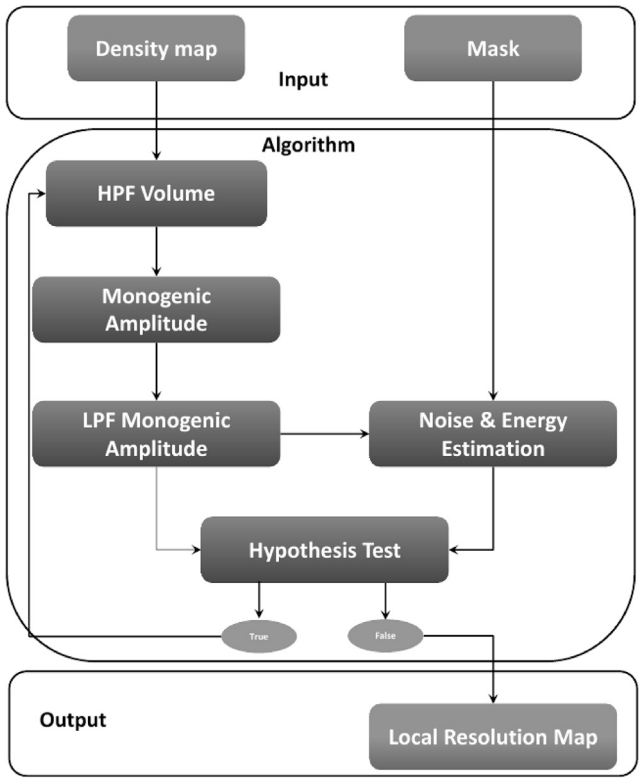

Figure 2. *MonoRes* Workflow

Input volumes, the algorithm (middle box blocks), and the result (i.e., the resolution map - down block). HPF, high-pass filter; LPF, low-pass filter.

Here, we present a fully automatic method for measuring local resolution. Our algorithm, *MonoRes*, is based on the use of monogenic signals, a mathematical generalization to several dimensions of the 1D analytic signals (Gabor, 1946). This kind of signal has special utility in those problems for which there is a need to decompose a function instantaneously (locally) into envelope and phase terms (Figure 1), for example, in signal processing (Potamianos and Maragos, 1994) or polarimetry (Gil, 2007).

Here, we provide a brief mathematical introduction for readers unfamiliar with Riesz and Hilbert transforms (Table 1). The algorithm starts by filtering the input map at a given frequency and then computes the monogenic signal, allowing extraction of the monogenic amplitude at this frequency, which is then compared with the monogenic amplitude distribution of noise at that resolution (Figures 2 and 3). This allows assessment whether, at that resolution and location, the monogenic amplitude observed is significantly higher than that expected from noise. Noise can be estimated by two volumes calculated from two halves of the data, or by considering voxels within a user-defined mask (as in *ResMap*). A deep explanation of the method is included in the STAR Methods. Results using *MonoRes* in a variety of situations confirm that (1) it is fully automatic and more rapid than existing approaches, (2) it is an accurate estimation as confirmed on structural maps with known resolutions, and (3) it provides a locally filtered map in addition to the local resolution estimation.

RESULTS

To test *MonoRes* performance, the method was applied to two computer-simulated maps and to four experimental maps. Analysis of computer-generated maps allowed us to confirm *MonoRes* performance in controlled situations for which the correct resolution was known, including local resolution changes. In the study of experimental maps, selected as examples of different use cases, we compared *MonoRes* with

Table 1. Comparison between Hilbert and Riesz (s_H – s_R) Transforms and between Analytic and Monogenic Signals

Concept	1D-Signal	3D-Signal
Transform	Hilbert $\widehat{s}_H(\omega) = -\frac{\omega}{\lvert\omega\rvert}\widehat{s}(\omega)$	Riesz $\widehat{s}_R(\vec{\omega}) = -\left(\frac{\omega_x}{\lVert\vec{\omega}\rVert^2}\widehat{s}(\vec{\omega}), \frac{\omega_y}{\lVert\vec{\omega}\rVert^2}\widehat{s}(\vec{\omega}) \frac{\omega_z}{\lVert\vec{\omega}\rVert^2}\widehat{s}(\vec{\omega})\right)$
Transformed signal	analytic signal $s_a(t)$ $s_a = s(t) + i\, s_H(t)$	monogenic signal $s_{MG}(\vec{r}) s_{MG}(\vec{r}) = s(\vec{r}) + i\, s_{Rx}(\vec{r}) + j\, s_{Ry}(\vec{r}) + k\, s_{Rz}(\vec{r})$
Amplitude	$A(t) = \sqrt{s^2(t) + s_H^2(t)}$	$A(\vec{r}) = \sqrt{s^2(\vec{r}) + s_R^2(\vec{r})}$

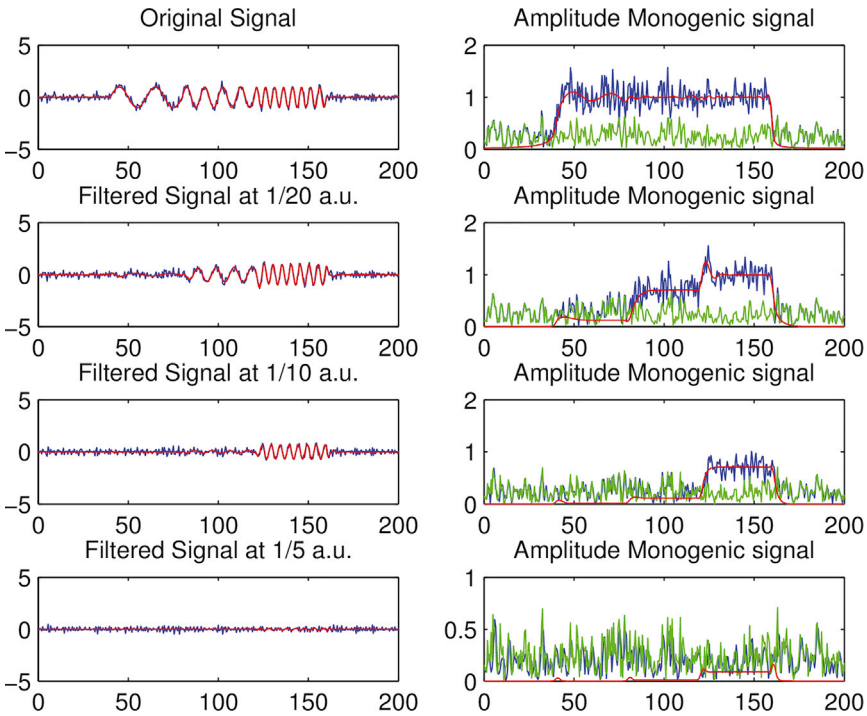

Figure 3. Filtered Signals at different frequencies and their Monogenic Amplitudes

Frequencies are shown on the left and amplitudes on the right. The monogenic amplitude of noise is indicated in green, signal or monogenic amplitude with added noise in blue, and without noise in red.

resolution results reported in the original publications, as well as with our own execution of *ResMap* and *blocres* (note that although the *ResMap* manual prewhitening step was performed to the best of our knowledge, its manual nature introduces variability that is intrinsically difficult to document; for *blocres*, default parameters were used). In all cases, we used a simple computational configuration, a single CPU core 2x-Xeon E5-2630 v3 2.40 GHz work station with 64 GB RAM.

MonoRes has been carefully integrated in *Xmipp* (de la Rosa-Trevín et al., 2013) and the image processing framework *Scipion* (de la Rosa-Trevín et al., 2016), with a simple interface and visualization options. Moreover, *MonoRes* is integrated into Scipion Web Tools (Conesa et al., 2017), a simple image processing website centered on specific workflows and addressed to non-expert users. In this way, *MonoRes* can be compared with other methods such as *ResMap* or *blocres* with no requirement for *Scipion* installation.

The inputs for the method are the original volume (or two half-volumes), a mask, and the resolution range to be evaluated. Other options can nonetheless be provided, such as a user request for output volume filtering at the local resolution filter, or the original map premasked inside a sphere. The output produces a resolution map that can be analyzed in *Scipion* v1.1. Different visualization options are provided for analyzing results (a resolution

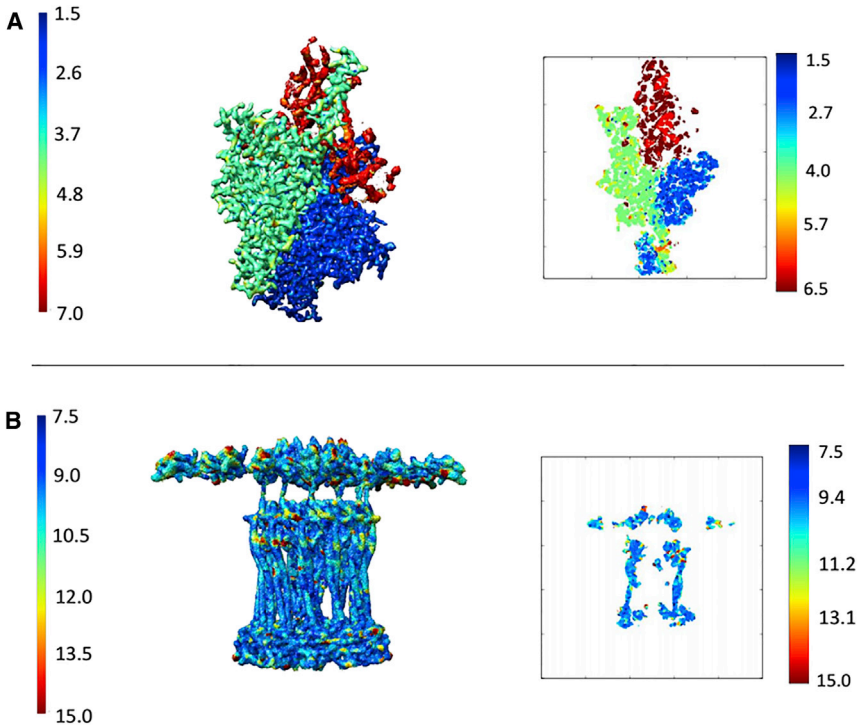

Figure 4. *MonoRes* Results for Synthetic Maps

(A) Glutamate dehydrogenase filtered at 2, 4, and 6 Å from the PDB: 5K12 atomic model.

(B) The synthetic large map (1,000 × 1,000 × 1,000) from the PDB: 3JC9 filtered at 10 Å. For (A and B) *MonoRes* resolution map (left), resolution slices obtained by *MonoRes* (right).

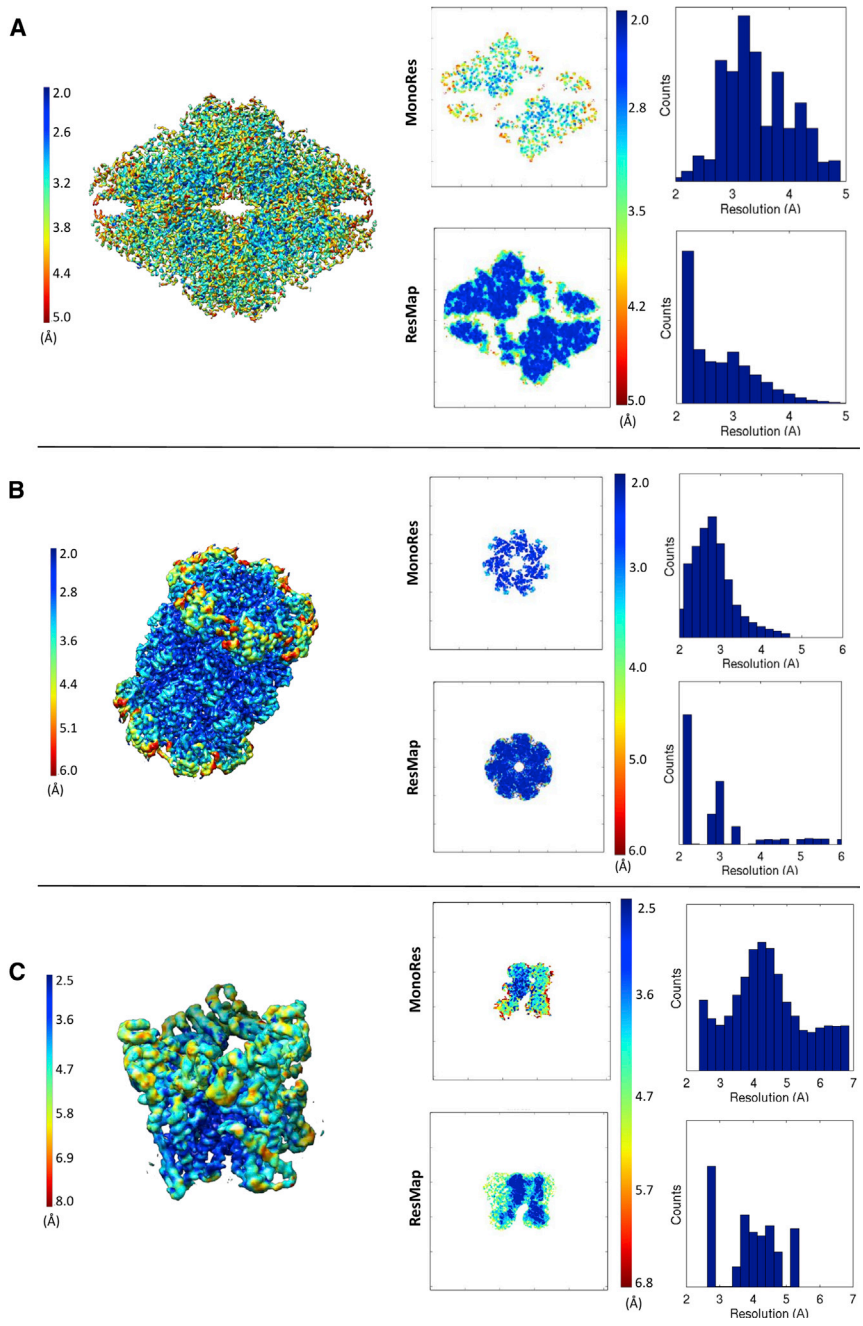

Figure 5. *MonoRes* Resolution Map, *MonoRes* and *ResMap* Resolution Slices, and Histograms for the Experimental Maps

(A–C) (A) β-galactosidase (EMDB-2984), (B) proteosome (EMDB-6287) and (C) TRPV1 (EMDB: EMD-5778). Resolution maps are on the left, *MonoRes* and *ResMap* resolution slices are in the middle, and histograms on the right.

histogram, the resolution map, colored slices of the resolution map, or the possibility of opening Chimera with the original map colored with the resolution values).

Tests with Computer-Simulated Data

Computer-Simulated Map 1: Glutamate Dehydrogenase

The first test case was based on the work of Merk et al. (2016). on glutamate dehydrogenase, starting from the PDB: 5K12 atomic model and generating a map with a sampling rate of 1 Å/pixel using *xmipp_volume_from_pdb* (Sorzano et al., 2015). This map is composed of six chains that were first grouped into pairs using *Chimera* (Pettersen et al., 2004) and then low-pass filtered at frequencies of 2, 4, and 6 Å with a raised cosine of 0.02 (in normalized units) before addition of Gaussian noise with zero mean and 0.08 SD. This implies that each pair of chains cannot show frequencies above 1.9, 3.6, and 5.0 Å, respectively.

The result of *MonoRes* application in Figure 4 shows how the method produces a resolution map with values near the expected cutoff frequencies of 2, 4, and 6 Å. As expected, the median of the local resolution estimations for each pair of chains corresponded to the value of the frequency filter applied to each chain, considering the filter transition band. The median values were thus 2.5, 4.0, and 6.5 Å, with SDs of 0.8, 0.6, and 0.6 Å, respectively. *MonoRes* is therefore very accurate, with local resolution values very similar to the expected theoretical values. Run time in our configuration was 30 s. The output exploration capabilities of *MonoRes* are very rich, and include direct visualization of the local resolution 3D map using Chimera as a result of its integration in *Scipion*.

Computer-Simulated Map 2: Type IVa Pilus

The second simulated case considered the atomic model of the type IVa pilus machine (PDB: 3JC9) (Chang et al., 2016), converted from the atomic model into a volume density map as before, specifying a sampling rate of 0.5 Å/pixel, which resulted in a large map of 1,000 × 1,000 × 1,000 voxels. This map was then low-pass filtered to 10 Å applying a transition band of 0.008 width (frequency units normalized to 0.5), i.e., Fourier coefficients are multiplied by 1 up to 10 Å, and the filter falls smoothly to 0 at 8.6 Å resolution. Finally, Gaussian noise was added to the map with zero mean and 0.08 SD.

The goal of this test was 2-fold: first to confirm that *MonoRes* reproduced the known resolution limit of the maps, and second, to assess the ability of the method to deal with large maps. Since the synthetic map was low-pass filtered at 10 Å, we expected the distribution of local resolution estimations to center around this value. This is clearly the case, as seen in Figure 4, where most voxel values are blueish, in accordance with the fact that the map was low-pass filtered to 10 Å. Quantitative analysis showed a median resolution value of 9.7 Å, with 0.5 Å

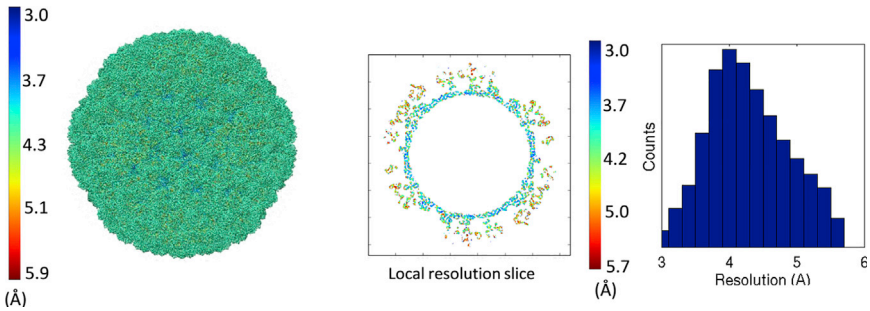

Figure 6. Local Resolution Results

MonoRes resolution map (left), and *MonoRes*, *ResMap*, and *blocres* resolution slices (center) and histograms (right) for the experimental half-maps of (A) β-galactosidase (EMDB: EMD-2984) and (B) proteosome (EMDB: EMD-6287).

SD. Macromolecule borders are very challenging sites for estimation of local resolution, since signal voxels are adjacent to noise voxels. This effect is especially pronounced at low resolution, at which there is inherently more intervoxel crosstalk, and tends to disappear at high resolution. *MonoRes* is in general very robust, but in this low-resolution example, with the map filtered to 10 Å, some voxels in the local map appear to indicate a resolution lower than 10 Å. While we cannot rule out that this is the case, we simply note that frontier voxels at low resolution can be problematic. This situation tends to resolve itself at high resolution, which reduces the practical importance of this issue. In computational time, *MonoRes* required 137 min for this large map.

Tests with Experimental Data

Experimental Map 1: β-galactosidase

The first experimental map used corresponds to the cryo-EM structure of β-galactosidase in complex with a cell-permeant inhibitor (EMDB: EMD-2984) (Bartesaghi et al., 2015). This map presents the highest resolution obtained in any cryo-EM study in 2015. It measures 292 × 292 × 292 voxels with a sampling rate of 0.637 Å/pixel. The original publication reported a resolution of 2.2 Å (gold standard FSC at 0.143). We calculated local resolution maps with *MonoRes* and *ResMap*, using the combination of final map plus a mask or two half-maps; *blocres* was also applied in the case of the two half-maps. The mask used was always the same, and was constructed by thresholding the macromolecular map. The results with the single and the two half-maps are shown in Figures 5A and 6, respectively.

When a single map is considered (Figure 5A), *MonoRes* local resolution ranges from 2.0 Å to 4.8 Å, with median at 3.3 Å and 0.6 Å SD. *ResMap* in turn reports a resolution range from 2.2 Å to 5 Å, with median at 2.6 Å and 0.6 Å SD. We also calculated the resolution difference between these two methods, and the results cast a median difference of 1.1 Å and an SD of 0.6 Å, with *MonoRes* reporting a lower resolution than *ResMap*; the histogram of this resolution difference is shown in Figure S1. The computational times were 3.0 and 5.3 min for *MonoRes* and *ResMap*, respectively.

The case involving two half-maps is shown in Figure 6A. Results are consistent with the local resolution maps using a single volume. *MonoRes* achieved a median resolution of 3.2 Å with 0.4 Å SD. *ResMap* reported a median resolution of 2.7 Å with 0.6 Å SD, and *blocres* determined a median resolution of 2.6 Å with 0.1 Å SD with a criterion of FSC at 0.5. The resolution difference was also calculated between *MonoRes* and these methods. The *MonoRes-blocres* difference presented a median value of 1 Å with 0.6 Å SD, while the *MonoRes-ResMap* difference shows a median value 1 Å of with 0.4 Å SD; the histograms of the resolution differences are shown in Figure S1. The reported median values of 2.6 Å or 2.7 Å imply that there are resolutions above and below the median. When a high-pass filter was applied below 2.6 Å (median value), hardly any structure was found, see Figure S2. *MonoRes* better identified this situation, as the percentage of voxels with resolution better than 2.6 Å was much smaller than for the other two algorithms, which implies that the other two algorithms might be incurring resolution inflation. The computational times were 6.3, 8.5, and 22.6 min for *MonoRes*, *ResMap,* and *blocres*, respectively.

In both figures (Figures 5 and 6), the areas with relatively higher and lower resolution are shown on the *MonoRes* volume on the left and on a representative slice through the volume in the center (for *MonoRes*, colored voxels are exclusively those inside the user-supplied mask), and correspond to the inside and outside of the macromolecule, as anticipated.

The absolute resolution estimation value for this map is not known, at difference from our study on computer-simulated data, and might be difficult to extrapolate from one resolution determination approach to another (Sorzano et al., 2017). We nonetheless note that *MonoRes* provides a simple-shaped, well-centered histogram of values that is easy to interpret, as is the local resolution map.

Experimental Map 2: Proteasome

The second experimental data example analyzed the map of the proteasome in the study reported as EMDB: EMD-6287 (Campbell et al., 2015). This volume is 300 × 300 × 300 voxels with a sampling rate of 0.982 Å/pixel. The reported resolution for this map was 2.8 Å (gold standard FSC at 0.143). Local resolution maps were determined using a single final map as well as two half-maps, and are shown in Figures 5B and 6B, respectively.

For the single final map, *MonoRes* estimated the resolution range to be from 2.0 Å to 4.6 Å, with median at 2.8 Å and a 0.5 Å SD, again with simple-shaped, well-centered value distribution. *ResMap* cast a resolution range from 2.2 Å to 6.0 Å, with median at 2.7 Å and 1.0 Å SD. The distribution of the resolution difference between the two methods had a median value of 0.4 Å and SD of 0.5 Å; the histograms of the resolution differences are shown in Figure S1. The computational times were 1.5 and 13.75 min for *MonoRes* and *ResMap*, respectively.

Results were similar when two half-maps were considered, as shown in Figure 5B. *MonoRes* determined a median resolution of 2.9 Å with 0.5 Å SD, *ResMap* had the same median resolution of 2.9 Å with 1.0 Å SD, and *blocres* achieved a median value of 3.0 Å

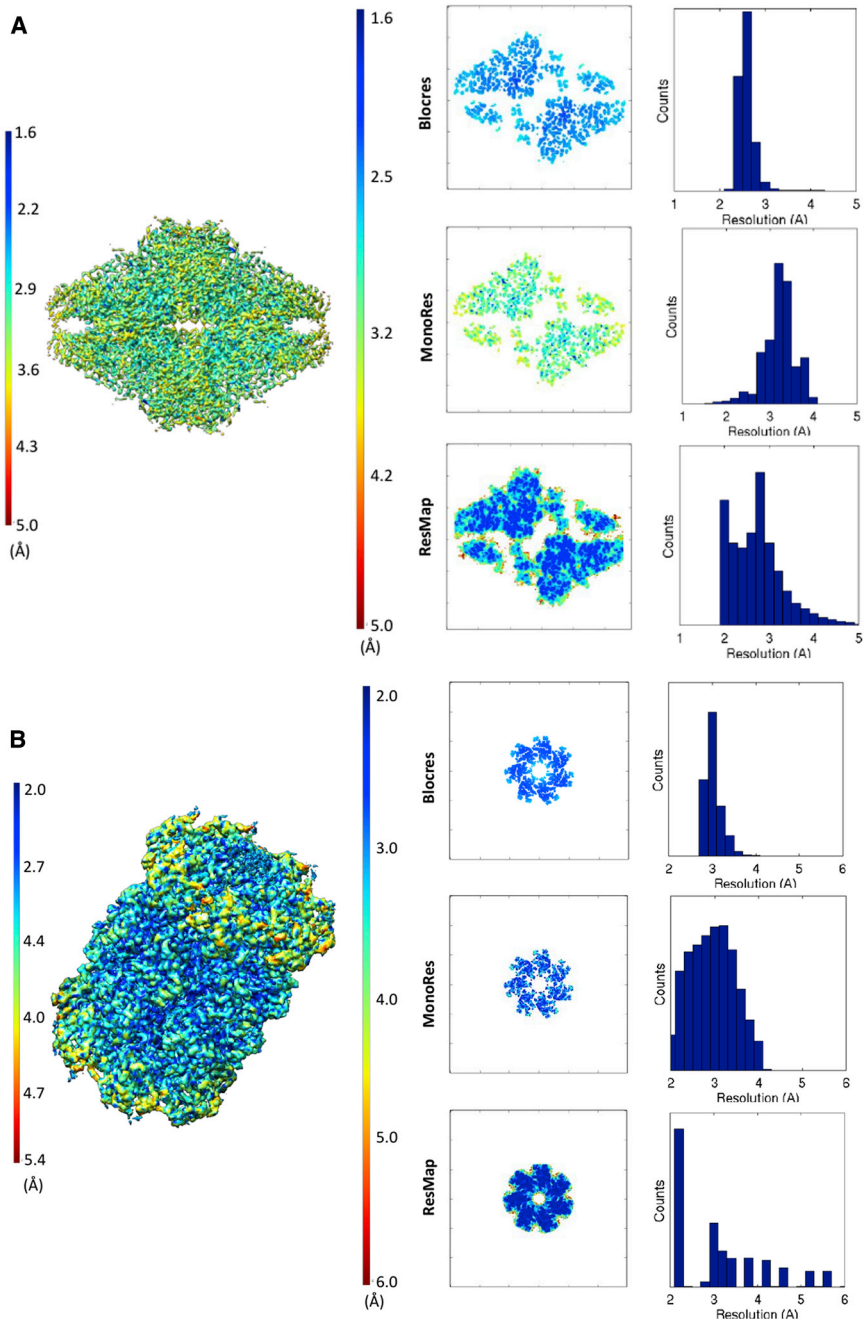

Figure 7. Local Filtering Results

(A) Original volume (top) and slice (bottom) of the TRPV1 (EMDB: EMD-5778).

(B) Volume locally filtered by its local resolution values.

(FSC criterion at 0.5) with 0.2 Å SD. Computational times were 2.75, 14.5, and 123.5 min for *MonoRes*, *ResMap,* and *blocres*, respectively. The resolution difference between *MonoRes* and *ResMap* was a median value of 0.6 Å with SD of 0.6 Å, whereas the difference between *MonoRes* and *blocres* showed a median of −0.03 Å and SD of 0.5 Å. Resolution differences are indicated in Figure S1. The result shows considerable similarity between *MonoRes* and *blocres* for this example. This map was also high-pass-filtered at 2.8 Å, the value of the median resolution reported by *MonoRes* and *ResMap*. The result shows structure at that resolution (Figure S2). This result explains the marked inter-method similarity in measurement for the proteasome.

Experimental Map 3: Capsaicin Receptor TRPV1

The third experimental case is the capsaicin receptor TRPV1 (EMDB: EMD-5778) (Liao et al., 2013). Images were acquired with sampling rate of 1.1 Å/pixel and a box size of 256 × 256 × 256 voxels for particle picking, reporting an FSC value of 3.8 Å at 0.143 gold standard. Local resolution was determined using a single map with *MonoRes* and *ResMap*; results are shown in Figure 5. Local resolution was computed in the interval from 2.0 Å to 8.0 Å. *MonoRes* yielded a median resolution of 4.2 Å with 1.1 Å SD, while *ResMap* reported a median local resolution of 4.0 Å with 0.8 Å SD. The median resolution difference was 0.8 Å with and SD of 0.95 Å. Histograms of these resolution differences are shown in Figure S1. This map represents an experimental case in which a wide range is expected. This wide range is clearly found in both methods and is reflected in the histogram of voxel resolution. In the case of *MonoRes*, however, the spread of local resolution voxel values is slightly larger and the overall results more conservative. We can use this example to introduce another degree of flexibility provided by *MonoRes*, that is, calculation of a map in which each pixel is filtered to its significant local resolution; this choice is presented in Figure 7. The computation time for *MonoRes* was approximately 2 min, and 9 min for *ResMap*.

Experimental Map 4: Aquareovirus

The fourth test case corresponds to an Aquareovirus (EMDB: EMD-5160) (Zhang et al., 2010). This map has a sampling rate of 1.1 Å/pixel, the size was 740 × 740 × 740 voxels, and the resolution reported by FSC at 0.143 gold standard was 3.2 Å. The *MonoRes* results shown in Figure 8 provide an easy-to-interpret map and representative slice, with a higher resolution core and a lower resolution periphery. The range of values for local resolution estimation ranged from 3.0 Å to 5.6 Å, with median at 4.2 Å and 0.6 Å SD, again with a simple histogram of values. The computation time for *MonoRes* was 13 min, while *ResMap*, in our computational platform, could not compute this volume due to its large size (*ResMap* results are therefore not shown in this case).

Table 2 summarizes the results of *MonoRes* and *ResMap* for the four experimental cases analyzed.

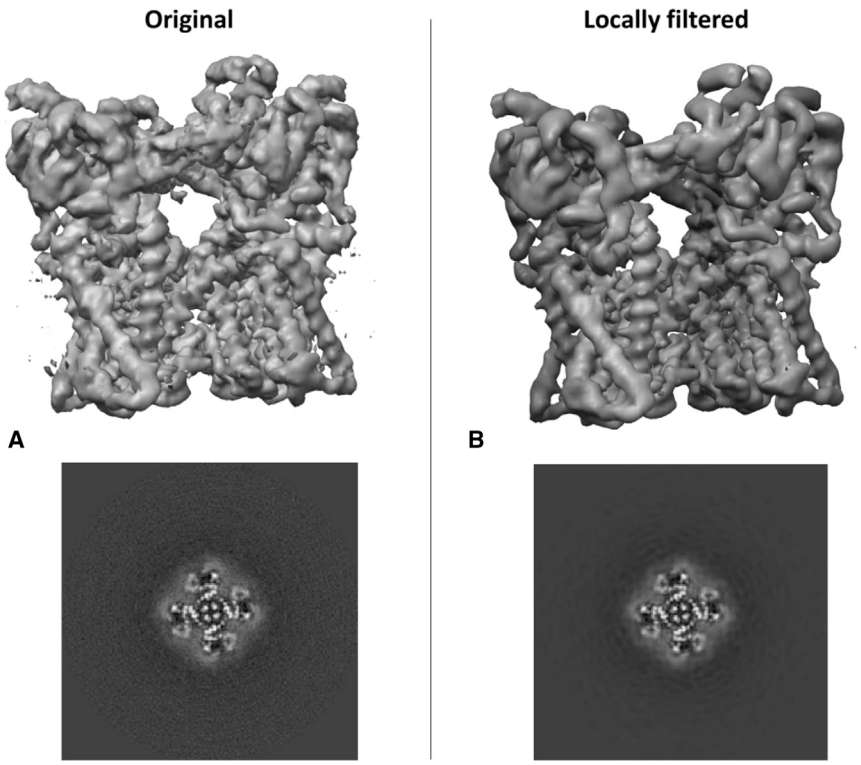

Figure 8. *MonoRes* Resolution Map, Resolution Slice, and Histogram Obtained for the Aquareovirus (EMDB: EMD-5160)

DISCUSSION

Here, we present a fully automatic method for determining local resolution of electron microscopy density maps. It is based on a conceptually simple approach, the estimation of signal amplitude on a per voxel basis coupled with hypothesis testing that evaluates whether the local energies observed differ significantly from those observed in noise. This approach naturally allows acquisition of a map in which each voxel is filtered to its significant resolution.

We present the results for computer-simulated data and experimental maps. The work on synthetic data is particularly relevant for a study that deals with the complex topic of resolution, which has been defined in many different ways in many different contexts (for a thorough recent review, see Sorzano et al., 2017). Probably, it may not be realistic to get all these different definitions of resolution to provide exactly the same values (see Table 2). For this reason, we undertook this study with in-depth analyses of some very clear, defined situations in which a specific value could be stated for "resolution." *MonoRes* excelled in these tests, and proved to be a very accurate approach that provided results very similar to those that known *a priori*. In addition, *MonoRes* is fully automatic, in that no user intervention is required, which avoids a possible source of result discrepancy linked intrinsically to manual interventions such as a prewhitening step (in fact, *MonoRes* is invariant in this case). An added convenience with regard to computational performance is that *MonoRes* allows calculation of the local resolution in large maps (as large as 1,000 × 1,000 × 1,000), more rapidly and with less memory consumption than current approaches.

As a local resolution estimation approach that is automatic, accurate, rapid, and able to provide locally filtered maps, *MonoRes* has the potential to open new fields of application, such as the consideration of local resolution in iterative refinement, in classification, and in fitting approaches. Moreover, the distributions of resolution differences show that *MonoRes* offers more conservative local resolution values than other methods, but coincides with test filtered maps, and avoids the background sensitivity of the FSC, rendering *MonoRes* an unbiased method. The algorithm is publicly available from *Xmipp* (http://xmipp.cnb.csic.es) and has been integrated into *Scipion* (http://scipion.cnb.csic.es) and the Scipion Web Tools (http://scipion.cnb.csic.es/m/services/).

STAR★METHODS

Detailed methods are provided in the online version of this paper and include the following:

- KEY RESOURCES TABLE
- CONTACT FOR REAGENTS AND RESOURCE SHARING
- METHOD DETAILS
  - A Brief Introduction to Analytic and Monogenic Signals

Table 2. Summary of Local Resolution for the Experimental Cases

Volume	FSC (Å)	*MonoRes* Range (Å)	*ResMap* Range (Å)	*Blocres* Range (Å)
β-Galactosidase	2.2	[2.0, 4.8] (3.3)	[2.2 5.0] (2.6)	–
(Using halves)	2.2	[1.6, 4.0] (3.2)	[2.0 5.0] (2.7)	[2.2, 4.2] (2.6)
Proteasome	2.8	[2.0, 4.6] (2.8)	[2.2, 6.0] (2.7)	–
(Using halves)	2.8	[2.0, 4.1] (2.9)	[2.2, 6.0] (2.9)	[2.8, 4.0] (3.0)
TRPV1	3.3	[3.5, 6.8] (4.2)	[2.7, 5.2] (4.0)	–
Aquareovirus	3.6	[3.0, 5.6] (4.2)	–	–

The number in parentheses is the local resolution median.

- On the Hilbert and Riesz Transform
- On the Analytic and Monogenic Signals
- Comparison Summary between Analytic/Hilbert and Monogenic/Riesz Terms
- MonoRes Method
- Local Resolution Estimation
- An Explanatory Unidimensional Example
- Local Filtering

SUPPLEMENTAL INFORMATION

Supplemental Information includes two figures and can be found with this article online at https://doi.org/10.1016/j.str.2017.12.018.

ACKNOWLEDGMENTS

The authors express their gratitude to Prof. Hemant Tagare for his interest and advice on this project. We thank C. Mark for editorial assistance. This work is supported by grants from the Madrid Regional Government (CAM S2010/BMD-2305), the Spanish Ministry of Economy and Competitiveness (AIC-A-2011-0638, BIO2013-44647-R, and BIO2016-76400-R), and the Fundación General CSIC (Programa ComFuturo).

AUTHOR CONTRIBUTIONS

Conceptualization, C.O.S.S.; Methodology, J.L.V., C.O.S.S., J.V., and J.M.C.; Software, J.L.V. and C.O.S.S.; Validation, J.G.-B., R. Melero, R. Marabini, J.M.R.-T., and J.O.; Formal Analysis, J.G.-B, R. Melero, R. Marabini, J.M.R.-T., and J.O.; Resources, J.C.; Writing, J.L.V., C.O.S.S., J.V., and J.M.C.; Visualization, J.G.-B. and P.C.; Supervision, C.O.S.S., J.V., and J.M.C.; Funding Acquisition, J.M.C.

Received: June 21, 2017
Revised: October 6, 2017
Accepted: December 29, 2017
Published: January 25, 2018

REFERENCES

Bartesaghi, A., Merk, A., Banerjee, S., Matthies, D., Wu, X.W., Milne, J.L.S., and Subramaniam, S. (2015). 2.2 Å resolution cryo-EM structure of β-galactosidase in complex with a cell-permeant inhibitor. Science *348*, 1147–1151.

Campbell, M., Veesler, D., Cheng, A., and Carragher, B. (2015). 2.8 Angstrom resolution reconstruction of the *Thermoplasma acidophilum* 20S proteasome using cryo-electron microscopy. Elife *4*, e06380.

Cardone, G., Heymann, J.B., and Steven, A.C. (2013). One number does not fit all: mapping local variations in resolution in cryo-EM reconstructions. J. Struct. Biol. *184*, 226–236.

Chang, Y.W., Rettberg, L.A., Treuner-Lange, A., Iwasa, J., Søgaard-Andersen, L., and Jensen, G.J. (2016). Architecture of the type IVa pilus machine. Science *351*, aad2001.

Conesa, P., Gutierrez, J., Quintana, A., de la Rosa-Trevín, J.M., Zaldívar-Peraza, A., Cuenca, J., Kazemi, M., Vargas, J., del Cano, L., Segura, J., et al. (2017). Scipion web tools: easy to use cryo-EM image processing over the web. Protein Sci. *27*, 269–275.

de la Rosa-Trevín, J.M., Otón, J., Marabini, R., Zaldívar, A., Vargas, J., Carazo, J.M., and Sorzano, C.O. (2013). Xmipp 3.0: an improved software suite for image processing in electron microscopy. J. Struct. Biol. *184*, 321–328.

de la Rosa-Trevín, J.M., Quintana, A., del Cano, L., Zaldívar-Peraza, A., Foche, I., Gutiérrez, J., Gómez-Blanco, J., Burguet-Castells, J., Cuenca, J., Abrishami, V., et al. (2016). Scipion: a software framework toward integration, reproducibility, and validation in 3D electron microscopy. J. Struct. Biol. *195*, 93–99.

Felsberg, M., and Sommer, G. (2001). The monogenic signal. IEEE Trans. Signal. Process. *49*, 3136–3144.

Gabor, D. (1946). Theory of communication. Proc. IEE (London) *93*, 429–457.

Gil, J. (2007). Polarimetric characterization of light and media. Eur. Phys. J. Appl. Phys. *40*, 1–47.

Harauz, G., and van Heel, M. (1986). Exact filters for general geometry three-dimensional reconstruction. Optik *73*, 146–156.

Kucukelbir, A., Sigworh, F.J., and Tagare, H.D. (2014). Quantifying the local resolution of cry-EM density maps. Nat. Methods *11*, 63–65.

Larkin, K.G., Bone, D.J., and Oldfield, M.A. (2001). Natural demodulation of two-dimensional fringe patterns. I. general background of the spiral phase quadrature transform. J. Opt. Soc. Am. A Opt. Image Sci. Vis. *18*, 1862–1870.

Liao, M., Cao, R., Julius, D., and Cheng, Y. (2013). Structure of the TRPV1 ion channel determined by electron cryo-microscopy. Nature *504*, 107–112.

Merk, A., Bartesaghi, A., Banerjee, S., Falconieri, V., Rao, P., Davis, M.I., Pragani, R., Boxer, M.B., Earl, L.A., Milne, J.L.S., and Subramaniam, S. (2016). Breaking cryo-EM resolution barriers to facilitate drug discovery. Cell *165*, 1698–1707.

Penczek, P.A. (2002). Three-dimensional spectral signal-to-noise ratio for a class of reconstruction algorithms. J. Struct. Biol. *138*, 36–46.

Pettersen, E.F., Goddard, T.D., Huang, C.C., Couch, G.S., Greenblatt, D.M., Meng, E.C., and Ferrin, T.E. (2004). UCSF Chimera–a visualization system for exploratory research and analysis. J. Comput. Chem. *25*, 1605–1612.

Potamianos, A., and Maragos, P. (1994). A comparison of the energy operator and the Hilbert transform approach to signal and speech demodulation. Signal Process. *37*, 95–120.

Saxton, W.O. (1978). Computer Techniques for Image Processing of Electron Microscopy (Academic Press), p. 289.

Saxton, W.O., and Baumeister, W. (1982). The correlation averaging of a regularly arranged bacterial envelope protein. J. Microsc. *127*, 127–138.

Scheres, S.H., and Chen, S. (2012). Prevention of overfitting in cryo-EM structure determination. Nat. Methods *9*, 853–854.

Sorzano, C.O., Marabini, R., Boisset, N., Rietzel, E., Schröder, R., Herman, G.T., and Carazo, J.M. (2001). The effect of overabundant projection directions on 3D reconstruction algorithms. J. Struct. Biol. *133*, 108–118.

Sorzano, C.O.S., Vargas, J., Otón, J., Abrishami, V., de la Rosa Trevín, J.M., del Riego, S., Fernández-Alderete, A., Martínez-Rey, C., Marabini, R., and Carazo, J.M. (2015). Fast and accurate conversion of atomic models into electron density maps. AIMS Biophys. *2*, 8–20.

Sorzano, C.O., Vargas, J., Otón, J., Abrishami, V., de la Rosa-Trevín, J.M., Gómez-Blanco, J., Vilas, J.L., Marabini, R., and Carazo, J.M. (2017). A review of resolution measures and related aspects in 3D electron microscopy. Prog. Biophys. Mol. Biol. *124*, 1–30.

Sousa, D., and Grigorieff, N. (2007). Ab initio resolution measurement for single particle structures. J. Struct. Biol. *157*, 201–210.

Unser, M., Sage, D., and Van De Ville, D. (2009). Multiresolution monogenic signal analysis using the Riesz-Laplace wavelet transform. IEEE Trans. Image Process. *18*, 2402–2418.

Unser, M., Sorzano, C.O., Thévenaz, P., Jonić, S., El-Bez, C., Carlo, S.D., Conway, J.F., and Trus, B.L. (2005). Spectral signal-to-noise ratio and resolution assessment of 3D reconstructions. J. Struct. Biol. *149*, 243–255.

Unser, M., Trus, B., and Steven, A.C. (1987). A new resolution criterion based on spectral signal-to-noise ratio. Ultramicroscopy *23*, 39–51.

Unser, M., and Van De Ville, D. (2010). Wavelet steerability and the higher-order Riesz transform. IEEE Trans. Image Process. *19*, 636–652.

Vargas, J., Abrishami, V., Marabini, R., de la Rosa-Trevín, J.M., Zaldivar, A., Carazo, J.M., and Sorzano, C.O.S. (2013a). Particle quality assessment and sorting for automatic and semiautomatic particle-picking techniques. J. Struct. Biol. *183*, 342–353.

Vargas, J., Otón, J., Marabini, R., Jonic, S., de la Rosa-Trevín, J.M., Carazo, J.M., and Sorzano, C.O. (2013b). FASTDEF: fast defocus and astigmatism estimation for high-throughput transmission electron microscopy. J. Struct. Biol. *181*, 136–148.

Zhang, X., Fang, Q., Hui, W.H., and Zou, Z.H. (2010). 3.3 Å cryo-EM structure of a nonenveloped virus reveals a priming mechanism for cell entry. Cell *141*, 472–482.

STAR★METHODS

KEY RESOURCES TABLE

REAGENT or RESOURCE	SOURCE	IDENTIFIER
Deposited Data		
Glutamate dehydrogenase	Merk et al., 2016	PDB-5K12
Type IVa pilus	Chang et al., 2016	PDB-3JC9
β-galactosidase Map	Bartesaghi et al., 2015	EMD-2984
Proteasome	Campbell et al., 2015	EMD-6287
TRPV1	Liao et al., 2013	EMD-5778
Aquareovirus	Zhang et al., 2010	EMD-5160
Software and Algorithms		
Scipion v1.0	de la Rosa-Trevín et al., 2016	http://scipion.cnb.csic.es
Xmipp3.0	de la Rosa-Trevín et al., 2013	http://xmipp.cnb.csic.es
xmipp_volume_from_pdb	Sorzano et al., 2015	http://xmipp.cnb.csic.es
MonoRes	This article	http://scipion.cnb.csic.es http://xmipp.cnb.csic.es
ResMap	Kucukelbir et al., 2014	
Blocres	Cardone et al., 2013	

CONTACT FOR REAGENTS AND RESOURCE SHARING

Further information and requests for reagents may be directed to, and will be fulfilled by the Lead Author, Dr. C.O.S. Sorzano (coss@cnb.csic.es) or J.L. Vilas (jlvilas@cnb.csic.es)

METHOD DETAILS

A Brief Introduction to Analytic and Monogenic Signals

The basis of *MonoRes* is to transform the original electron density map into another map that expresses signal strength at that location. This new map is termed a monogenic amplitude map; the transformation needed to obtain it is the Riesz transform (or Hilbert transform for 1D signals) (Unser and Van De Ville, 2010).

On the Hilbert and Riesz Transform

The Riesz transform can be understood as the generalization to multiple dimensions (N-D) of the Hilbert transform, which is only defined for 1D signals. One of the best approaches to understanding the Hilbert transform is perhaps via its relationship with the Fourier transform. Consider an arbitrary 1D function f(t), the Fourier transform, $\widehat{f}(\omega) = FT[f(t)]$, allows the original function to be decomposed as a combination of waves with different frequencies, ω. The Hilbert transform applied to the Fourier transform performs a shift of $+\pi/2$ to the negative frequencies and of $-\pi/2$ to the positive frequencies, or mathematically expressed,

$$FT[H(f(t))] = -i \cdot \mathrm{sign}(\omega)\widehat{f}(\omega), \qquad \text{(Equation 1)}$$

where i is the imaginary unit. A very simple case is a sinusoidal function, $f(t) = \cos(\omega \cdot t)$, whose Hilbert transform will be the function $H[f(t)] = \sin(\omega \cdot t)$, which exactly presents a shift of $\pm\pi/2$ for negative and positive frequencies, respectively. Considering a function that can be expressed in a Fourier series, the Hilbert transform will thus be such that the sines are exchanged for negative cosines and the cosines are changed to sines.

We would like to use in N-dimensional signals the advantages of the analytic signal to extract amplitude and phase in 1D. There is nonetheless no unique generalization of the Hilbert transform. One of the 2D extensions of this kind of signal is strongly connected to the spiral phase transform (Larkin et al., 2001; Vargas et al., 2013a, 2013b), and there are several extensions of the Hilbert transform to higher dimensions. Here we used the Riesz transform (Felsberg and Sommer, 2001; Unser and Van De Ville, 2010; Unser et al., 2009), which is found by solving a Cauchy problem for the Poisson equation (Felsberg and Sommer, 2001). The Riesz transform is defined in the Fourier domain as

$$\widehat{s}_R(\omega) = -\frac{\omega}{\|\vec{\omega}\|}\widehat{s}(\vec{\omega}) = -\left(\frac{\omega_1}{\|\vec{\omega}\|}\widehat{s}(\vec{\omega}), \frac{\omega_2}{\|\vec{\omega}\|}\widehat{s}(\vec{\omega}), \ldots, \frac{\omega_N}{\|\vec{\omega}\|}\widehat{s}(\vec{\omega})\right), \qquad \text{(Equation 2)}$$

where $\hat{s}$ denotes the Fourier transform of the signal **s**, **ω** is the multidimensional frequency variable, and ω_j is its j-th component. Note the resemblance between the Fourier definition of the Hilbert transform and of the Riesz transform.

On the Analytic and Monogenic Signals

An analytic signal is defined as a complex signal without negative frequencies and with the real part equal to the original signal. Analytic signals, $s_a(t)$, are constructed from a given function, f(t), via the Hilbert transform as follows,

$$s_a(t) = s(t) + is_H(t)), \quad \text{(Equation 3)}$$

where $s_H(t)$ is the Hilbert transform of the original signal. The Hilbert transform thus allows a quadrature amplitude modulation of s(t). Note that this complex function can be rewritten in an exponential form, using the Euler formula, $s_a(t)=A(t)\cdot\exp[\phi(t)]$, where A(t) is termed amplitude of the analytic signal, and ϕ(t) is a phase term, specifically,

$$A(t) = \sqrt{s^2(t) + s_H^2(t)}. \quad \text{(Equation 4)}$$

An example of this decomposition is shown in Figure 1. The monogenic signal similarly constitutes the generalization to N-D of the unidimensional concept of analytic signals.

Let us illustrate the concept of analytic signal with some examples.

1. Consider the signal $s(t) = A\cos(\omega\cdot t)$, with $\omega>0$ and A is a real number, its Hilbert transform is $s_H(t) = A\sin(\omega\cdot t)$; therefore, the analytic signal is given by $s_a(t) = A[\cos(\omega\cdot t) + i\sin(\omega\cdot t)] = A\exp[i\omega\cdot t]$. As a consequence, the original signal, s(t), has been decomposed into two factors, an envelope or amplitude, A, and a term that contains only the phase, $\exp[i\omega t]$. Note that the imaginary part of $s_a(t)$ is the original function with a phase shift of $\pi/2$.
2. Consider now the signal $s(t) = \cos(3t)\exp[-(t-8)^2/10]$. The signal, its Hilbert transform (note the $\pi/2$ phase-shift with respect to the signal, as above), and its amplitude are shown in Figure 1. Note how the amplitude coincides with the envelope of the original function. Hence, the signal has been successfully decomposed into phase and amplitude.

We can extend these ideas to N dimensions through the concept of the monogenic signal, which is defined as

$$s_{MG}(\vec{r}) = s(\vec{r}) + \sum_{j=1}^{N} i_j\left[(s_R)_j(\vec{r})\right], \quad \text{(Equation 5)}$$

where i_j is the N-dimensional generalization of the complex unity. This generalization uses a Clifford algebra with N ''imaginary units'', i_j, that verify the properties $i_j^2 = -1$, $i_j i_k = -i_k i_j$ (complex numbers and quaternions are particular cases of a Clifford algebra for N = 1 and N = 3, respectively).

We now calculate the monogenic amplitude as

$$A(\vec{r}) = \sqrt{s^2(\vec{r}) + \sum_{j=1}^{N} s_{Rj}^2(\vec{r})}. \quad \text{(Equation 6)}$$

Comparison Summary between Analytic/Hilbert and Monogenic/Riesz Terms

To better illustrate the extrapolation from unidimensional concepts to several dimensions, a comparison of 1D and 3D is summarized in Table 1. The spatial location is represented by **r** and the frequency vector by $\boldsymbol{\omega} = (\omega_x, \omega_y, \omega_z)$, where the subindex x, y, or z defines the direction along which the frequency is measured.

MonoRes Method

The objectives of *MonoRes* were to produce a map, as large as the original map, in which each voxel provides an estimate of local resolution, and to render a structural map locally filtered to the estimated local resolution. A mask determines where the particle is, allowing separation of the particle (inside the mask) and the noise (outside the mask). The input volume is thus high pass-filtered at many frequencies, followed by computation of the local monogenic amplitude at each frequency. The statistical distributions of monogenic amplitudes of noise and signal can be determined using the mask. For all points inside the mask, a hypothesis test is then used to verify whether the null hypothesis is satisfied (i.e., that the local monogenic amplitude at a given voxel/location and frequency arises from the noise distribution and not the signal distribution). Finally, the resolution value for each position/voxel will be given by the highest frequency at which the test determines that the local amplitude arises from the signal and not from the noise. The false positive rate is also controlled. A hypothesis test is performed for each voxel; when a voxel does not pass the test, the algorithm allows its resolution to be computed in the next iteration, i.e., for a higher frequency. To assign a resolution value, a voxel must thus fail the hypothesis test twice, which considerably reduces the false positive rate.

Local Resolution Estimation

The algorithmic inputs to *MonoRes* are two, a signal map and a noise map. The signal map is considered to be the original map of the macromolecule, V(**r**), inside a user-specified mask. The noise map, in turn, can be specified in two ways, either as those voxels of the macromolecular map outside the mask or, better still, by providing two half-maps of the macromolecule, $V_1(\mathbf{r})$ and $V_2(\mathbf{r})$, in the context of the so-called ''gold standard'' approach for resolution estimation (Scheres and Chen, 2012).

The basis of the algorithm is a frequency sweep from low to high. At each frequency, we determine whether the local monogenic amplitude at a voxel is significantly different from the monogenic amplitude observed for the noise. To do this, we establish a threshold from the noise distribution for all the hypothesis tests performed within the mask at this frequency value. Local resolution is defined as the reciprocal of the first frequency for which the voxel amplitude of the macromolecule fails to be significantly above noise. The algorithmic steps of our method are given below and shown in Figure 2.

1. *High pass filter.* The original map is high pass-filtered at a specific frequency, ω_0, and a filtered map, $V_{HPF,\omega 0}(\mathbf{r})$ is then obtained (HPF, high pass-filtered) (see Figure 2 legend). Once the true resolution of the map at a given point is passed, a voxel within the structure should not be distinguishable from a background voxel.
2. *Monogenic amplitude.* With the high pass-filtered map, the monogenic signal is calculated via the Riesz transform

$$V_{R,\omega_0}(r) = FT^{-1}\left[-\frac{\omega}{\|\vec{\omega}\|}\widehat{V}_{HPF,\omega_0}(\vec{\omega})\right], \qquad \text{(Equation 7)}$$

where $V_{R,\omega 0}(\mathbf{r})$ is the Riesz transform of $V_{HPF,\omega 0}(r)$; note that $V_{R,\omega 0}(\mathbf{r})$ is a vectorial function, with components $V^j_{R,\omega 0}(\mathbf{r})$ for j = 1,...,3 (number of dimensions). From the Riesz transform, the monogenic amplitude, $A_{MG,\omega 0}$, is therefore obtained as

$$A_{MG,\omega_0}(\vec{r}) = \sqrt{\left(V_{HPF,\omega_0}\right)^2(\vec{r}) + \sum_{j=1}^{3}\left(V^j_{R,\omega_0}\right)^2(\vec{r})}. \qquad \text{(Equation 8)}$$

The advantage of monogenic signals is the possibility of writing them as complex exponentials, i.e., in a wave form. It allows amplitude and phase terms to be separated. The amplitude of the wave is called the monogenic amplitude; its expression is shown in Table 1. Note that the input high pass filter allows selection of the wave frequencies.

3. *Low pass-filtering the monogenic amplitude.* The monogenic amplitude is low pass-filtered to the frequency $\boldsymbol{\omega_0}$**.** This step smooths the monogenic amplitude, which due to the non-linear nature of the square root, has high-frequency components not of interest for our purposes.
4. *Estimation of the distribution of the monogenic amplitude in noise.* This step is to determine the distribution of the monogenic amplitudes of noise voxels. The method for estimating this distribution depends on the input, i.e., whether there is a single density map or if two half-maps are provided.
   a) *Single volume*: When a background mask is provided, it defines a frontier that separates the map background (noise) from the macromolecule (signal). The noise histogram is then determined using all voxels outside the mask.
   b) *Two half-maps*: This method requires that both halves be aligned. A noise volume is estimated as $(V_1(\vec{r}) - V_2(\vec{r}))/\sqrt{2}$ (the $\sqrt{2}$ factor guarantees that the power of the estimated noise volume is the same as the noise power in each of the individual volumes). In this noise volume, we are not restricted to the background mask, and can use the whole volume instead.
5. *Determination of local resolution.* For each voxel inside the masked volume, we compute whether its local monogenic amplitude is larger than the 1-α percentile of the distribution of monogenic amplitudes in noise, i.e., a hypothesis test. In this case, the signal is detectable in that voxel at the filtering frequency. A resolution map is thus created, and that frequency is assigned to the voxel. The noise threshold, ε, for the hypothesis test is defined as the mean noise plus the semi-length of the confidence interval as

$$\varepsilon = CDF^{-1}_{A_N}(1-\alpha),$$

where CDF_{AN} is the cumulative distribution function of the monogenic amplitudes of noise and we are considering a significance of 1-α (typically, 1-α = 0.95 is used). This step can be accelerated by approaching the noise distribution by a Gaussian distribution:

$$\varepsilon = \mu_n + CDF^{-1}_{N(0,1)}(1-\alpha)\sigma_n,$$

where μ_n is the mean of the monogenic amplitudes of noise, σ_n its standard deviation, and $CDF_{N(0,1)}$ is the cumulative density function of the standardized normal distribution.

Note that *MonoRes* is invariant with respect to radially symmetric filters, and there is thus no need for a pre-processing step like power spectral whitening. Another consequence is that the local resolution estimated by *MonoRes* is invariant to B-factor corrections.

Computing time is related to particle size rather than the size of the box in which the particle is found. The mask determines the number of voxels where there is signal. In terms of memory use, *MonoRes* requires approximately five copies of the volumes: the Fourier transform of the original volume, mask, resolution volume, monogenic amplitude, and an auxiliary volume.

An Explanatory Unidimensional Example

To illustrate the method clearly in a simple case, we generated a one-dimensional signal. The signal was composed by three sinusoidal functions at frequencies of 1/20, 1/10 and 1/5 a.u. (arbitrary units), assembled one after the other. This guarantees three regions at resolutions of 20, 10 and 5 a.u. Gaussian noise with a standard deviation of 0.2 was then added. The *MonoRes* algorithm consists of a high pass-filter frequency sweep and calculation of the corresponding monogenic amplitude of the filtered signal; the filtered signals are shown (Figure 3, left) with their respective monogenic amplitudes (Figure 3, right). In thi illustrative example, the monogenic amplitude of noise (green line) was obtained from the added signal of noise, computed with volumes only outside the mask. The monogenic amplitude is related to the signal energy; thus, in the top row in Figure 3, the monogenic amplitude has the shape of a rectangular window, the same length as the signal. The monogenic amplitude of the noise is also plotted (green). As expected, the amplitude of the noise is constant and lower than the signal (note that the amplitude range has been modified to improve visibility in Figure 3, bottom row). When a high pass filter at 1/20 a.u. is applied, however, the first, lowest frequency of the signal disappears; as a result, it can be measured in the monogenic amplitude. The monogenic amplitude of the signal in the region of the filtered frequency cannot be distinguished from noise (hypothesis test), and the resolution value of the last filter frequency can be assigned to that region. This procedure can be repeated until the monogenic signal cannot be distinguished from noise.

Local Filtering

Noise is usually one of the main drawbacks in the analysis of electron density maps. A global low pass filter at the FSC value is therefore commonly applied at the end of the reconstruction process, although a better alternative would be to use the local resolution map to define local filters adapted to each voxel.

MonoRes implements local filtering in a very straightforward manner by taking advantage of high pass filtering to compute the monogenic amplitude at each frequency. The locally filtered map uses the intermediate volumes $V_{LPF,\omega 0}(\mathbf{r}) = V(\mathbf{r})\text{-}V_{HPF,\omega 0}(\mathbf{r})$. Finally, the locally filtered volume at each location $\mathbf{r}$ is equal to $V_{LPF,\omega 0}(\mathbf{r})$, being $\omega_0(\mathbf{r})$ the resolution estimated for that location.